THE ASTROPHYSICAL JOURNAL, 789:75 (11pp), 2014 July 1
doi:10.1088/0004-637X/789/1/75

© 2014. The American Astronomical Society. All rights reserved. Printed in the U.S.A.

NuSTAR OBSERVATIONS OF THE MAGNETAR 1E 2259+586

Julia K. Vogel[1], Romain Hascoët[2], Victoria M. Kaspi[3], Hongjun An[3], Robert Archibald[3],
Andrei M. Beloborodov[2], Steven E. Boggs[4], Finn E. Christensen[5], William W. Craig[1,4], Eric V. Gotthelf[2],
Brian W. Grefenstette[6], Charles J. Hailey[2], Fiona A. Harrison[6], Jamie A. Kennea[7], Kristin K. Madsen[6],
Michael J. Pivovaroff[1], Daniel Stern[8], and William W. Zhang[9]

[1] Physics Division, Physical and Life Sciences Directorate, Lawrence Livermore National Laboratory, Livermore, CA 94550, USA
[2] Physics Department and Columbia Astrophysics Laboratory, Columbia University, New York, NY 10027, USA
[3] Department of Physics, McGill University, Montreal, Quebec H3A 2T8, Canada
[4] Space Sciences Laboratory, University of California, Berkeley, CA 94720, USA
[5] DTU Space, National Space Institute, Technical University of Denmark, Elektrovej 327, DK-2800 Lyngby, Denmark
[6] Cahill Center for Astronomy and Astrophysics, California Institute of Technology, Pasadena, CA 91125, USA
[7] Department of Astronomy and Astrophysics, Pennsylvania State University, University Park, PA 16802, USA
[8] Jet Propulsion Laboratory, California Institute of Technology, Pasadena, CA 91109, USA
[9] Goddard Space Flight Center, Greenbelt, MD 20771, USA
Received 2014 February 24; accepted 2014 May 19; published 2014 June 17

ABSTRACT

We report on new broad band spectral and temporal observations of the magnetar 1E 2259+586, which is located in
the supernova remnant CTB 109. Our data were obtained simultaneously with the *Nuclear Spectroscopic Telescope
Array (NuSTAR)* and *Swift*, and cover the energy range from 0.5–79 keV. We present pulse profiles in various energy
bands and compare them to previous *RXTE* results. The *NuSTAR* data show pulsations above 20 keV for the first
time and we report evidence that one of the pulses in the double-peaked pulse profile shifts position with energy.
The pulsed fraction of the magnetar is shown to increase strongly with energy. Our spectral analysis reveals that the
soft X-ray spectrum is well characterized by an absorbed double blackbody or blackbody plus power-law model in
agreement with previous reports. Our new hard X-ray data, however, suggest that an additional component, such as
a power law, is needed to describe the *NuSTAR* and *Swift* spectrum. We also fit the data with the recently developed
coronal outflow model by Beloborodov for hard X-ray emission from magnetars. The outflow from a ring on the
magnetar surface is statistically preferred over outflow from a polar cap.

Key words: pulsars: individual (1E 2259+586) – stars: magnetars – stars: neutron – X-rays: bursts

Online-only material: color figures

1. INTRODUCTION

Magnetars are a class of young, isolated neutron stars (NSs). Their defining features are their sporadic outbursts in X-rays and soft gamma rays along with luminosities often much larger than their expected spin-down-powered X-ray emission. To date, 21 confirmed magnetars and 5 candidates have been reported[10] (Olausen & Kaspi 2014). Spin periods for magnetars lie in the narrow range of $P = 2.1$–11.8 s with period derivatives of the order of $\dot{P} = 10^{-11}$ s s^{-1}. The characteristic ages of these objects ($\tau = P/2\dot{P}$) imply that magnetars are rather young NSs with ages of the order of several thousand years. However, especially for young objects, the spin-down-inferred age is only a crude estimate. The young ages are, however, generally supported for most magnetars by their specific locations as well as their association with supernova remnants (SNRs). Both magnetar outbursts and a substantial fraction of their persistent X-ray emission are believed to be powered by their intense magnetic fields (Thompson & Duncan 1993, 1996), with strengths of 10^{14}–10^{15} G inferred assuming magnetic dipole braking in vacuum ($B \propto \sqrt{P\dot{P}}$).

The magnetar model was originally formulated to explain the behavior of a sub-class of magnetars, the so-called soft gamma repeaters (SGRs), the most active of these objects. However, observations of similar behavior such as bursting activity (Gavriil et al. 2002; Kaspi et al. 2003) for anomalous

X-ray pulsars (AXPs), another previously identified magnetar sub-class, indicate that SGRs and AXPs are likely to be at different ends of a continuous magnetar activity spectrum.

One of the most studied magnetars to date is 1E 2259+586. It was the first AXP to be discovered (Fahlman & Gregory 1981, 1983) and also played a key role in the unification of these NSs with very high magnetic fields, when it exhibited a series of over 80 X-ray bursts in 2002 (Kaspi et al. 2003). This AXP has shown a very stable spin-down rate (Kaspi et al. 1999) as well as pulsed flux emission apart from glitches[11] in 2002 and 2007 (Icdem et al. 2012; Dib & Kaspi 2014) and a rare antiglitch in 2012 (Archibald et al. 2013). 1E 2259+586 is located near the center of SNR CTB 109 (G109.1 − 1.0), which is known for its half-shell morphology in both radio and X-rays (see Figure 1). It is at a distance of 4.0 ± 0.8 kpc (Tian et al. 2010). The spin period of 1E 2259+586 is $P = 6.98$ s with a spin-down rate of $\dot{P} = 0.05 \times 10^{-11}$ s s^{-1}. This implies a surface dipole magnetic field of 0.59×10^{14} G, which is toward the lower end of the typical range of magnetar magnetic fields, and the characteristic age is estimated to be 230 kyr. While no radio counterpart at the position of the X-ray pulsar has been identified down to a level of 7μJy (Archibald et al. 2013), persistent emission has been detected from the mid- to far-infrared, all the way up to X-rays (see, e.g., Kuiper et al. 2006 for a brief review of

---

[10] http://www.physics.mcgill.ca/~pulsar/magnetar/main.html

[11] A glitch is a sudden spin-up of a neutron star. In one case a sudden spin-down has been observed (Archibald et al. 2013), which is referred to as an antiglitch.
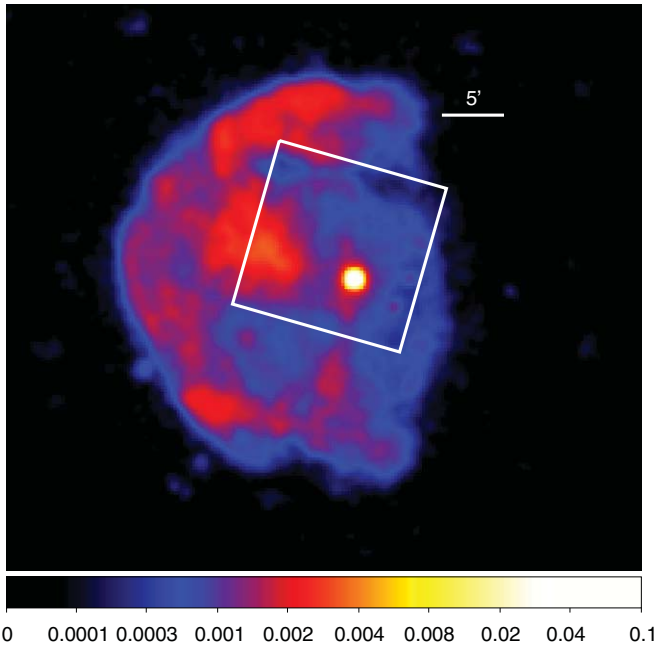
Figure 1. *ROSAT* PSPC image of SNR CTB 109 (0.1–2.4 keV). The white frame indicates the *NuSTAR* field of view (FoV), but no corresponding data have been included here. The bright point source is the magnetar 1E 2259+586.

(A color version of this figure is available in the online journal.)

previous observations). The soft X-ray spectrum is typical of AXPs and, in the 0.5–7.0 keV band, was described by Patel et al. (2001) as a blackbody (BB) spectrum with temperature $kT = 0.412(6)$ keV and a soft power law (PL) with $\Gamma = 3.6(1)$ for $N_H = 0.93(3) \times 10^{22}$ cm^{-2}. Zhu et al. (2008) updated these values in the 0.6–12.0 keV band with *XMM-Newton* data taken post-outburst in 2002, yielding $kT = 0.400(7)$ keV and $\Gamma = 3.75(3)$ for $N_H = 1.012(7) \times 10^{22}$ cm^{-2}. It is interesting that significant spectral changes were observed by Woods et al. (2004) at energies <10 keV when comparing pre- and post-burst data for the 2002 outburst. Timing and spectral properties for hard X-ray emission (8–24 keV) from 1E 2259+586 were first derived by Kuiper et al. (2006) using *RXTE* data. They also compared their results for the pulsed spectrum to upper limits from *IBIS* ISGRI and *COMPTEL* (Den Hartog et al. 2006). For the *RXTE* data, an absorbed double PL model yields a good fit to the pulsed spectrum with soft and hard PL indices of $\Gamma_1 = 4.26(1)$ and $\Gamma_2 = -1.02^{+0.24}_{-0.13}$ for $N_H = 0.93(3) \times 10^{22}$ cm^{-2}. Therefore, this AXP follows others in exhibiting an onset of dramatic hardening above 10 keV. For 1E 2259+586, Kuiper et al. (2006) found that the PL components become equally strong at $E = 15.8 \pm 2.3$ keV. For energies beyond 20 keV, conclusive confirmation of the dramatic hardening for 1E 2259+586 has not been available until now.

In this paper, we report on the spectral and temporal properties of the magnetar 1E 2259+586 in the 0.5–79 keV band. Our analysis is based on data acquired with the *Nuclear Spectroscopic Telescope Array* (*NuSTAR*) and the *Swift* X-Ray Telescope (XRT). In Section 2, we describe the observations, and following this we present the results of our data analysis in Section 3. We apply the coronal outflow model of Beloborodov (2013a) to the hard X-ray emission data, and show that the model is consistent with the phase-resolved spectra. A discussion of our results can be found in Section 4, and in Section 5 we conclude and summarize our findings.

Table 1
NuSTAR and *Swift* Observations of 1E 2259+586 Used in This Study

Observatory	Mode	ObsID	Date (MJD)[a]	Date	Exp (ks)
NuSTAR	⋯	30001026002	56406	2013 Apr 24	37.3
NuSTAR	⋯	30001026003	56407	2013 Apr 25	15.4
NuSTAR	⋯	30001026005	56408	2013 Apr 26	16.3
NuSTAR	⋯	30001026007	56428	2013 May 16	88.4
Swift	PC	00080292002	56407	2013 Apr 25	13.1
Swift	PC	00080292003	56408	2013 Apr 26	14.1
Swift	PC	00080292004	56410	2013 Apr 28	2.7

Note. [a] At the start of data acquisition.

2. INSTRUMENTS AND OBSERVATIONS

NuSTAR is the first hard X-ray focusing telescope in space with sensitivity in the energy range of 3–79 keV (Harrison et al. 2013). The instrument consists of two co-aligned focusing optics (Hailey et al. 2010) with CdZnTe detectors in the focal plane (Harrison et al. 2010). Each focal-plane module consists of four detector chips and the two telescope modules are dubbed FPMA and FPMB. *NuSTAR*'s energy resolution is 400 eV at 10 keV (FWHM) and the observatory provides an angular resolution of 58″ HPD[12] (18″ FWHM). Its temporal resolution of 2 μs is more than adequate for studying the 6.98 s AXP 1E 2259+586. For more information on *NuSTAR*, see Harrison et al. (2013).

Swift (Gehrels et al. 2004) is a multi-wavelength mission dedicated to the study of gamma-ray bursts. The *Swift* XRT (Burrows et al. 2005) is one of three instruments flown on the satellite. It is a Wolter-I type optic with a charge-coupled device (CCD) focal plane detector. The instrument is sensitive in the energy range from 0.2 to 10 keV with an energy resolution of 140 eV at 5.9 keV and a point-spread function of 22″ (HPD) at 8.1 keV.

The *NuSTAR* observations of 1E 2259+586 began on 2013 April 24 at UT 21:51:07 with the last of four observations concluding on 2013 May 18 at UT 06:01:07. The total net exposure for the combination of all four observations is 157.4 ks. A simultaneous *Swift* observation (XRT, photon-counting mode) was carried out to extend the spectral coverage down to ∼0.5 keV. While *NuSTAR* is very sensitive in the hard X-ray band, the low-energy data from the *Swift* XRT (0.2–10 keV) improve our ability to constrain the thermal components which are softer and emit mostly below the *NuSTAR* pass-band. The *Swift* observation started at UT 00:23:55 on 2013 April 25 and was split into three parts with a total exposure time of 29.9 ks.

The *NuSTAR* data were processed using the standard *NuSTAR* Data Analysis Software `NuSTARDAS` version 1.2.0 along with CALDB version 20131007 and HEASOFT version 6.13 as available on HEASARC.[13] For the *Swift* data, cleaned event files were produced using `xrtpipeline` along with the HEASARC remote CALDB[14] employing the standard filtering procedure of Capalbi et al. (2005). Further processing steps applied to these files are outlined below. Details about the different observations are shown in Table 1, which summarizes all data sets used in this analysis. Figure 2 shows the unsmoothed, exposure-corrected *NuSTAR* image of 1E 2259+586 in two energy bands, chosen to yield a comparable number of counts in the signal extraction region of radius 60″.

---

[12] Half-power diameter.
[13] See http://heasarc.gsfc.nasa.gov
[14] See http://heasarc.nasa.gov/docs/heasarc/caldb/caldb_remote_access.html
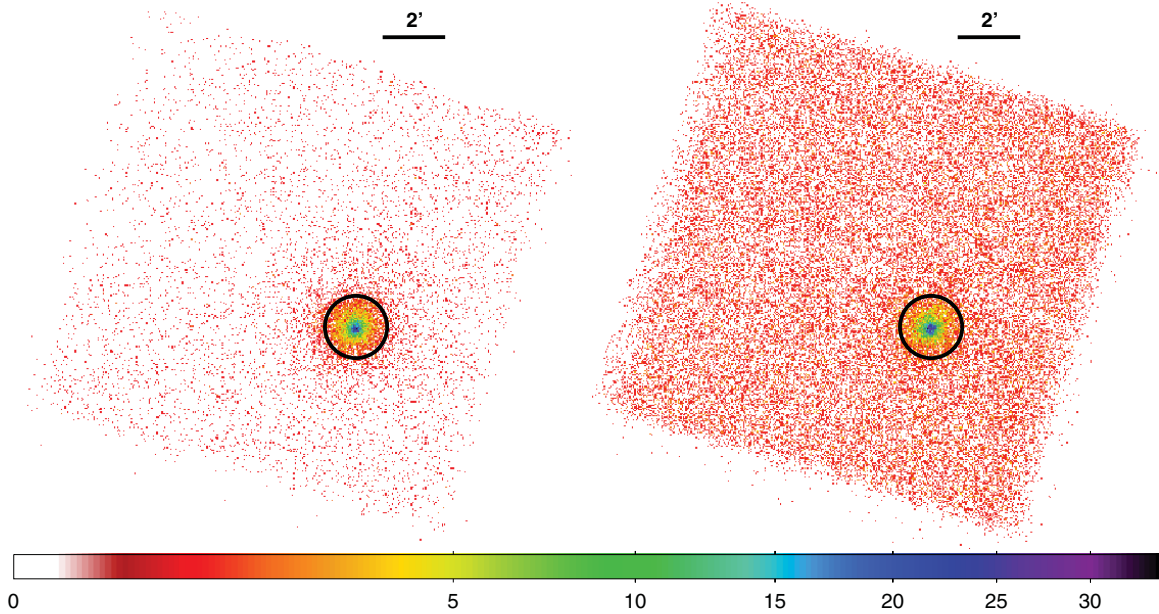
Figure 2. Images of unsmoothed, exposure-corrected *NuSTAR* data in two energy ranges (left: 3–4 keV, right: 4–79 keV) with comparable numbers of counts in the signal extraction region of 60″ radius.

(A color version of this figure is available in the online journal.)

3. ANALYSIS AND RESULTS

3.1. Timing Analysis

For the timing analysis, we extracted photons in a circular region of 60″ radius around the nominal source position for the *NuSTAR* data, while for *Swift* we used a 22″ radius. The energy bands used for spectral analysis were 5–79 keV and 0.5–10 keV for *NuSTAR* and *Swift*, respectively. Since 1E 2259+586 is located in CTB 109, the SNR background must be considered. Sasaki et al. (2004) pointed out that no emission above 4 keV was observed in the *Chandra* data apart from the pulsar and the *NuSTAR* data agrees with this. Since in one of the two *NuSTAR* modules (FPMA) stray light is observable at the edge of the field of view, we excluded this region when defining the background extraction area. For *NuSTAR*, background was extracted from a circular region of radius 100″ nearby the source region. We also compared our results using these background regions to those obtained using the mission's background model nuskybgd (Wik et al. 2014), and confirmed that all results were compatible within the corresponding uncertainties.

Due to the good spatial resolution of the *Swift* XRT, background could be extracted from an annular region around the NS with an inner radius of 80″ and an outer radius of 200″. Before continuing we checked if any pile-up events were present in the data. We followed the standard *Swift* procedure[15] and determined the count rate in a circular region of 47″.2 radius (20 pixels) centered on the source to be above 0.5 counts s^{-1}, indicating that the central 1–2 pixel radius region of the bright core might suffer from pile-up. We removed this area for the subsequent analysis by substituting the circular source extraction region by an annulus with inner and outer radii of 5″ and 22″, respectively. We also re-generated the ARFs to correct the flux of the spectrum for the loss of counts due to the use of an annular region as well as the correction factor for the light curves.[16]

Table 2
Swift Ephemeris for 1E 2259+586 Archibald et al. (2013)

Parameter	Value
Spin frequency, f_0 (s^{-1})	0.14328414235(81)
Spin frequency derivative, $\dot{\nu}_0$ (s^{-2})	$-10.14(12) \times 10^{-15}$
Epoch	MJD 56250.000
Start observing epoch	MJD 56201.284
Stop observing epoch	MJD 56439.246

In the next step, we applied a barycentric correction to the selected source events using the multi-mission tool barycorr with the corresponding orbital and clock correction files at the *Chandra* position of $\alpha = 23^h01^m08^s.295$ and $\delta = +58°52'44''.45$ (J2000.0) reported by Patel et al. (2001). Following the H-test method (De Jager et al. 1989), we searched for pulsations and determined the best period for the significant pulsations to be $P(NuSTAR) = 6.97914(2)$ s and $P(Swift) = 6.97915(2)$ s. The measured periods were in agreement with those obtained from the ephemeris of the *Swift* monitoring program of 1E 2259+586 (see Table 2).

The resulting pulse profiles are shown in Figure 3 for six energy ranges: 3–4 keV, 4–8.3 keV, 8.3–11.9 keV, 11.9–16.3 keV, 16.3–24.0 keV, and 24.0–79.0 keV. The bands up to 24.0 keV were chosen to coincide with those reported by Kuiper et al. (2006) for direct comparison. All pulse profiles, with the exception of the highest energy band (24–79 keV), are background-subtracted. The statistical significance of the observed pulsations in all energy bands is larger than 99% (*p* value[17] smaller than 0.01). For the lower five energy bands, the pulse profiles agree generally with those reported by Kuiper et al. (2006); however, in the energy ranges between 11.9 and 24.0 keV slight differences are apparent. In the highest energy band (24–79 keV), significant pulsations are observable

---

[15] See http://www.swift.ac.uk/analysis/xrt/pileup.php
[16] See http://www.swift.ac.uk/analysis/xrt/arfs.php

[17] The *p* value is the probability of obtaining a test statistic which is at least as extreme as the one that was actually observed under the assumption that the null hypothesis (in our case, no pulsation) is true.
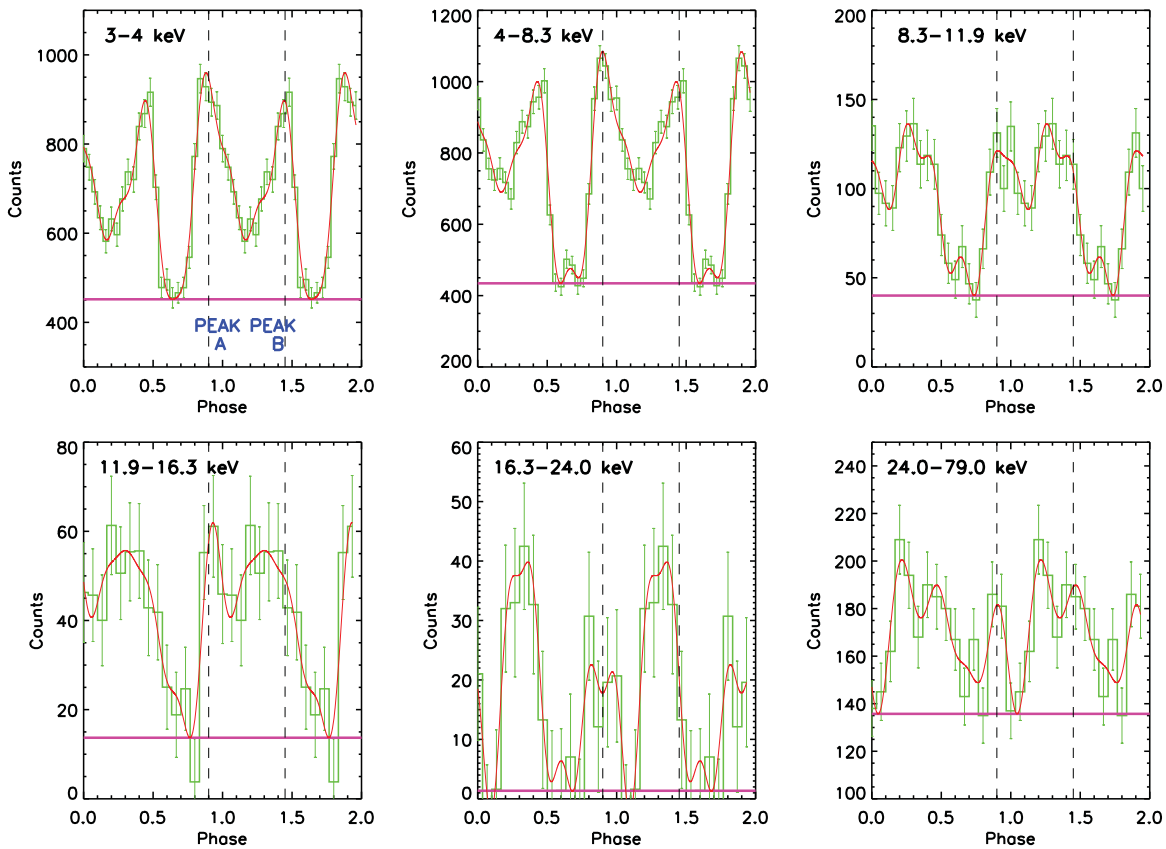
Figure 3. Pulse profiles for 1E 2259+586 from *NuSTAR* data in various energy bands. All but the pulse profile in the band from 24–79 keV, which has limited statistics, are background-subtracted. Energy bands up to 24 keV were chosen to enable direct comparison with Kuiper et al. (2006). The dashed lines near phase 0.9 and 1.45 are meant to serve as a guide to the eye to compare alignment of peak A and peak B. Note that the *y*-axis labels differ and the zero is suppressed in some of the plots. Also shown is the Fourier representation of the pulse profiles (red) used to estimate the pulsed emission level, denoted by the horizontal line.

(A color version of this figure is available in the online journal.)

for the first time. We note, however, that due to limited statistics we did not subtract the background in order to avoid negative bin counts. The nominal background count rate in this case is 6.56×10^{-4} counts s^{-1}.

As previously pointed out by Kuiper et al. (2006), there is a gradual change in pulse morphology observable with increasing energy. The double-peak profile at low energies (below ∼8 keV) evolves into a less pronounced double peak or possibly a single-peak profile for intermediate energies (about 8–16 keV) and back to a double-peak structure at higher energies. A possible way to describe this development is that while for energies below ∼8 keV, the pulse near phase 0.9 (peak A") tends to dominate, it becomes less significant for increasing energy with respect to the second peak ("peak B") near phase 1.45. In the intermediate energy range (8–16 keV), both peaks are approximately equally pronounced, while peak B starts to slightly dominate at energies above ∼16 keV. A difference between *NuSTAR* and *RXTE* profiles is apparent in the energy bands of 11.9–16.3 keV and 16.3–24.0 keV. While Kuiper et al. (2006) observe a clearly dominating peak B in this energy range, our analysis shows only a small lead for this pulse over peak A.

In order to quantify the energy dependence of the pulse morphology, we decompose the pulse profiles in terms of their Fourier components. This decomposition is shown in Figure 4. We find six harmonics to be sufficient, and we included these in the plots. We observe that the ratio of the second harmonic to the first harmonic changes with energy. For energies below about 8 keV, the second harmonic dominates over the first, while in the

intermediate range of 8–16 keV the first harmonic takes the lead, before the second harmonic dominates again for 16–24 keV. If the main contribution originates from the first harmonic number, this indicates that there is either one single peak in the pulse profile or a double peak with maxima of similar magnitude, while a leading second harmonic number points toward a double peak with pulses of different height and/or shape. This Fourier decomposition therefore reflects the change in dominance of one peak over the other in the double-peak morphology or, likewise, a possible change from a two-peak structure to one peak and back. For the *NuSTAR* band ($E > 24$ keV), the first and third harmonics dominate (2, 4, and 6 contribute at the 10% level). When interpreting this power spectrum (lower right plot of Figure 4) one should keep in mind that background was not subtracted and the peak-to-valley ratio is not very large. Here the first and (small) second harmonic take care of the wide peak B (from phase 1–1.8, including the small feature in the main minimum), while the third harmonic describes the narrower, subdominant peak A.

As previously reported by Kuiper et al. (2006) as well as Gavriil et al. (2002), a small pulse-like feature can be observed in the main minimum around phase 0.60–0.65. This feature is the main reason for the presence of higher orders of harmonics ($n \geqslant 3$) in the Fourier decomposition (see Figure 4) of the pulse profile.

We also note that there is a hint of a small feature in the intermediate minimum between peak A and B around phase 1.2, best seen in the lowest two energy bands. With the
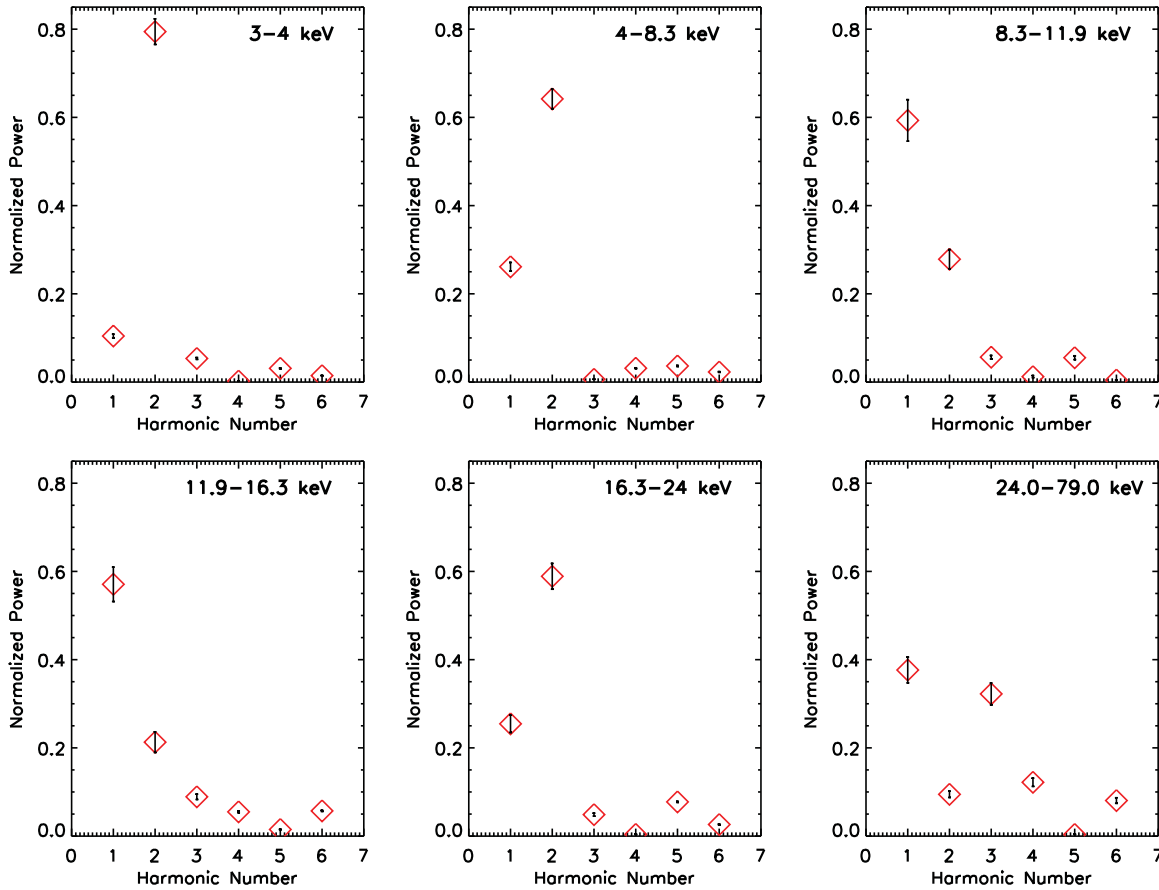
Figure 4. Evolution of the Fourier power harmonic distribution of the pulse profile for 1E 2259+586 as a function of energy. The energy bands shown correspond to those displayed in Figure 3. Power levels have been normalized to the total power of the first six harmonics. Note that the error bars for the 24–79 keV band are artificially small, since the corresponding pulse profile has not been background-subtracted. Errors will significantly increase in this energy band (due to low statistics) if background is taken into consideration.

(A color version of this figure is available in the online journal.)

Table 3
Mean Peak Position for Peaks A and B in Various Energy Bands

Energy Band (keV)	Position Peak A	Error Peak A	Position Peak B	Error Peak B
3.0–4.0	0.93	<0.01	1.39	<0.01
4.0–8.3	0.94	<0.01	1.38	<0.01
8.3–11.9	0.94	0.01	1.35	0.01
11.9–16.3	0.94	0.01	1.35	0.01
16.3–24.0	0.93	0.01	1.36	0.01

current statistics, however, we do not consider this feature to be significant.

Another observation is a possible shift of the peak B position in phase toward lower values with increasing energy. Dashed lines near phase 0.9 and 1.45 have been added to Figure 3 to guide the eye for alignment comparison of peak A and peak B. In order to test this pulse-shift hypothesis we determined the mean value of the peak position for each peak in various energy bands by considering the unbinned group phase between phase 0.75–1.1 for peak A and 1.2–1.55 for peak B. In addition, we crosschecked our results by fitting a Gaussian to the peaks. The results for the mean and its error are listed in Table 3 and indicate that peak A remains at the same phase position of 0.937(17) throughout all energy ranges (0.933(3) for $E \lesssim 8$ keV, 0.940(16) for $E \gtrsim 8$ keV). For peak B, there is a slight tendency to change position toward lower phase values for higher energies. Below

~8 keV, peak B can be found at 1.384(3), above these energies it is located at 1.349(17). We note that the shift is not very significant at the given statistics, and more data are needed to confirm or rule out the observed tendency.

In addition, we used the ephemeris-folded profiles to determine the pulsed fraction (PF) as a function of energy for our observations. A pulse profile that changes with energy or time makes it challenging to determine the PF of the source accurately and different methods are commonly used in the literature (see, e.g., Archibald et al. 2007, A. M. Archibald et al. 2014, in preparation for a discussion). All of them have their advantages and disadvantages and therefore there are some caveats to keep in mind. The area PF is probably the most natural and physically meaningful definition. It is defined as the difference between the pulsed flux and the constant flux integrated over a full phase cycle and can be calculated according to

$$\mathrm{PF_{area}} = \frac{\frac{1}{N}\sum_{j=1}^{N} p_j - p_{\min}}{\frac{1}{N}\sum_{j=1}^{N} p_j}, \qquad (1)$$

where p_j is the number of events in the jth phase bin, N is the total number of bins, and $p_{\min}$ is the minimum flux. Note that the determination of the true minimum and its error is the main challenge and the biggest caveat when using $\mathrm{PF_{area}}$, because both noise and binning show a tendency to bias the values of the area PF upward. In Figure 3 we included the results
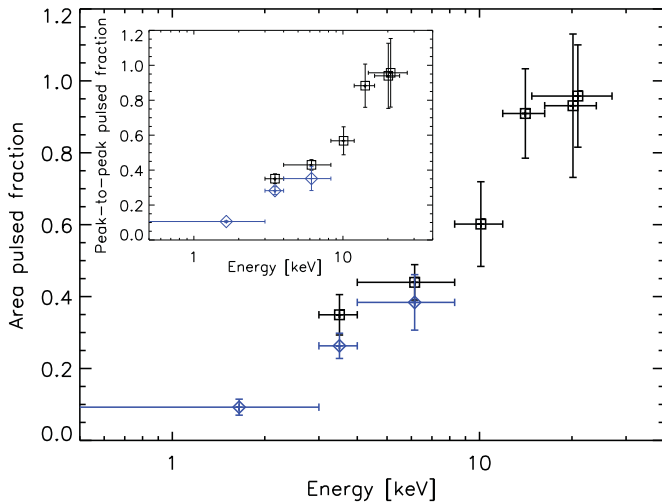
Figure 5. Area-pulsed fraction as function of energy for 1E 2259+586 from *NuSTAR* (black squares) and *Swift* data (blue diamonds). The energy bands correspond to those presented in Kuiper et al. (2006) for the *RXTE* PCA and HEXTE data. The small inset plot shows the conventionally defined PF$_\mathrm{P2P}$. In both cases the pulsed fraction strongly increases with energy.

(A color version of this figure is available in the online journal.)

Figure 6. rms deviation of the flux from the mean as a function of energy for 1E 2259+586 from *NuSTAR* (black squares) and *Swift* data (blue diamonds). The energy bands correspond to those presented in Kuiper et al. (2006) for the *RXTE* PCA and HEXTE data. Similarly to the area and peak-to-peak pulsed fraction the PF$_\mathrm{rms}$ also strongly increases with energy, even though the absolute values differ due to the definition of the rms estimator.

(A color version of this figure is available in the online journal.)

for p_min as the minimum off-pulse value determined from the Fourier representation (horizontal magenta line). The results for the area PF using the p_min determined in this way are shown in Figure 5. Note that the *NuSTAR* energy bands here (black squares) correspond to those presented in Kuiper et al. (2006) for the *RXTE* Proportional Counter Array (PCA, five bands in the range from 3.0–24.0 keV) and HEXTE data (14.8–27.0 keV). The *Swift* data (blue diamonds) covers the two lowest *RXTE* PCA bands in Kuiper et al. (2006) plus an additional band from 0.3–3.0 keV. Background was subtracted in all energy bands.
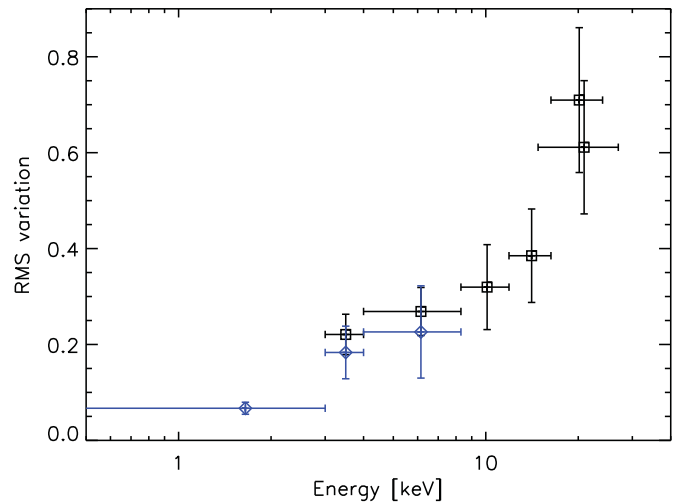
The small inset plot in the same figure displays the standard PF (peak-to-peak PF), conventionally defined as ratio of peak flux minus minimum flux to the total flux

$$\mathrm{PF}_\mathrm{P2P} = \frac{F_\mathrm{max} - F_\mathrm{min}}{F_\mathrm{max} + F_\mathrm{min}}. \tag{2}$$

This quantity is extensively used in the literature since it is straightforward to calculate, although the difficulty in determining the maximum and minimum flux values accurately is biased in a way similar to the area PF. Furthermore, the PF$_\mathrm{P2P}$ cannot provide information on the total energy since the peak width does not feed into the flux variation. The PF$_\mathrm{area}$ and PF$_\mathrm{P2P}$ derived from our data agree with each other within uncertainties and show the same trend: the PF increases dramatically with increasing energy. For energies around 10 keV, PF$_\mathrm{area}$ is 60% ± 12%, while for energies around 20 keV the fraction reaches 96% ± 14%.

Following the method presented in Gonzalez et al. (2010; see also the forthcoming publication by A. M. Archibald et al. 2014, in preparation for details), we additionally used a root-mean-square (rms) estimator as a measure for the deviation of the pulsed flux from its mean defined as

$$\mathrm{PF}_\mathrm{rms} = \frac{\sqrt{2 \sum_{k=1}^{6} \left((a_k^2 + b_k^2) - (\sigma_{a_k}^2 + \sigma_{b_k}^2) \right)}}{a_0}, \tag{3}$$

where the Fourier coefficients a_k and b_k are

$$a_k = \frac{1}{N} \sum_{j=1}^{N} p_j \cos\left(\frac{2\pi k j}{N}\right), \tag{4}$$

$$b_k = \frac{1}{N} \sum_{j=1}^{N} p_j \sin\left(\frac{2\pi k j}{N}\right) \tag{5}$$

and σ_{a_k}, σ_{b_k} are the uncertainties of a_k and b_k, respectively,

$$\sigma_{a_k}^2 = \frac{1}{N^2} \sum_{j=1}^{N} \sigma_{p_j}^2 \cos^2\left(\frac{2\pi k j}{N}\right), \tag{6}$$

$$\sigma_{b_k}^2 = \frac{1}{N^2} \sum_{j=1}^{N} \sigma_{p_j}^2 \sin^2\left(\frac{2\pi k j}{N}\right). \tag{7}$$

p_j is again the number of events in the jth phase bin, σ_{p_j} is the uncertainty of p_j, and N is the total number of bins. The number of Fourier harmonics included is $n = 6$. Note that PF$_\mathrm{rms}$ is the rms deviation of the flux from its average and can be defined in the Fourier domain. It does not cover the full range of values from 0–1 without additional (pulse shape dependent) renormalization, i.e., it is not a PF in the conventional sense, even though it is often referred to as the rms PF in the literature. This definition yields a very robust measure for the pulsed power that is less sensitive to noise and therefore significantly less biased than the area PF and more meaningful than the peak-to-peak PF. Figure 6 shows the rms variation for *NuSTAR* (black squares) and *Swift* data (blue diamonds). Note that the energy bands again correspond to those presented in Kuiper et al. (2006) for the *RXTE* PCA (five bands in the range from 3.0–24.0 keV) and HEXTE data (14.8–27.0 keV) and represent background-subtracted data in all energy bands. Since the definition of PF$_\mathrm{rms}$ differs from those of PF$_\mathrm{area}$ and PF$_\mathrm{P2P}$ as mentioned above, PF$_\mathrm{rms}$ does not have the same values as the other definitions in each energy band, but the same trend is observable in all cases:

the PF increases dramatically with increasing energy. Without renormalization we determined that the PF_{rms} is $32\% \pm 9\%$ for energies around 10 keV, while for energies around 20 keV it reaches $71\% \pm 15\%$.

3.2. Spectral Analysis

3.2.1. Phase-averaged Spectral Analysis

In this section, we use the *Swift* and *NuSTAR* observations to derive a phase-averaged spectrum. The same extraction regions as defined in Section 3.1 were used and pile-up for the *Swift* data was corrected for as described above.

We started with fitting the *Swift* data only in order to compare the results to previous soft X-ray measurements (Zhu et al. 2008) as well as to obtain a best-fit N_H to be used for the combined of *Swift* and *NuSTAR* data sets. All extracted spectra were grouped to have at least 50 counts per bin using the grppha tool. We fit the resulting spectra with XSPEC v12.8.1 using an absorbed BB plus PL model (tbabs*(bbody+powerlaw)) as well as an absorbed double BB (tbabs*(bbody+bbody)). The *Swift* spectrum is a little softer ($\Gamma = 4.1(1)$) than previously reported ($\Gamma = 3.75(3)$; Zhu et al. 2008), but consistent within uncertainties with these earlier results. Our best-fit result yields $N_H = 1.10(6) \times 10^{22}$ cm^{-2} in the case of the BB plus PL and $N_H = 0.60(4) \times 10^{22}$ cm^{-2} for the double-BB model. The first value agrees well with estimates of Durant & van Kerkwijk (2006) obtained from fitting individual absorption edges of O, Fe, Ne, Mg, and Si in the *XMM-Newton* Reflection Grating Spectrometer spectra. The latter value is in agreement with Zhu et al. (2008) and consistent with the best-fit N_H value for CTB 109, $N_H = (0.5–0.7) \times 10^{22}$ cm^{-2}, as measured by Sasaki et al. (2004).

In a next step we fit the spectra from 0.5–79 keV by using the *NuSTAR* and *Swift* data sets together. All model parameters were tied except for the cross-normalization factors, which were set to 1.0 for *NuSTAR*'s FPMA and left to vary for FPMB and *Swift*. Spectra were rebinned to have at least 50 counts per bin. We started out with fitting an absorbed double BB (tbabs*(bbody+bbody)) but the fit was poor, yielding a χ^2 per degree of freedom (dof) of 1448/827. The fit improved slightly by using an absorbed BB plus PL (tbabs*(bbody+powerlaw)), with χ^2 over dof of 1152/827. Adding an additional component improved the fit significantly and therefore a more complex model (BB+double PL or BB+broken PL, χ^2/dof = 689/825 or 747/825, respectively) than suggested by previous data was favored. The *F*-test supports this conclusion, yielding a probability significantly smaller than 0.05. All spectral fit results can be found in Table 4, while Figure 7 shows our best-fit model for the spectra of *NuSTAR* and *Swift*.

3.2.2. Phase-resolved and Pulsed Spectral Analysis

In this section we present results from a phase-resolved spectral analysis based on the *NuSTAR* and *Swift* data to study the double-peak structure of the pulse profiles shown in Figure 3. The phase intervals containing peak A and peak B were chosen to be 0.80–1.16 and 1.16–1.52, respectively. The off-peak spectrum covers the range of phase 0.52–0.80. Before fitting the spectra we used grppha to regroup the data such that there are at least 50 counts per spectral bin. We also use the same cross-normalization factors as obtained for the phase-averaged spectroscopy (*NuSTAR*: 1.0 for FPMA, 1.06 for FPMB; *Swift*: 0.94) and froze them for this fit along with the N_H value obtained
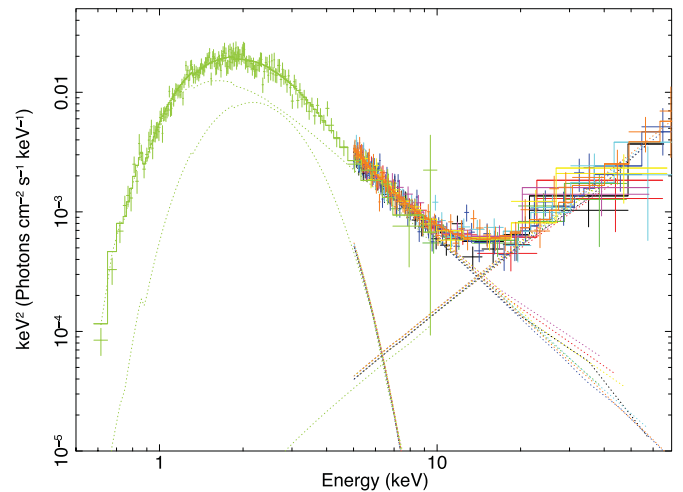
Figure 7. Phase-averaged spectra of *Swift* data (green) and all four *NuSTAR* observations with the best-fit model (see Table 4). The additive components are included in the plot. The model shown is an absorbed blackbody plus a double power law.

(A color version of this figure is available in the online journal.)

above for the BB+PL model ($N_H = 1.10(6) \times 10^{22}$ cm^{-2}). To compare the spectra of the three phase intervals, we fit them with an absorbed BB plus a broken PL model or a BB plus a double PL. All fit results are included in Table 4. Some of the spectral parameters differ slightly for the three chosen phase ranges: the photon indices are slightly harder for peak B than they are for peak A and the softest PL is obtained for the off-peak spectra. The BB temperatures for all three regions are consistent and the break point for the energy of the broken PL fit is located around 10 keV.

We also investigated the pulsed spectrum by subtracting the unpulsed emission from the total emission, but the statistics are too low to extract conclusive results. We cannot rule out a simple PL or confirm a hardening at high energies (above ~15 keV) as suggested by Kuiper et al. (2006).

3.2.3. Spectral Fits with the Coronal Outflow Model

Similar to what was done by An et al. (2013) for *NuSTAR* observations of 1E 1841−045, we apply the coronal outflow model of Beloborodov (2013a) to the observations of 1E 2259+586. In this model the hard X-ray component is produced by a decelerating $e^\pm$ outflow in a twisted magnetic loop (the "j-bundle"). The relativistic $e^\pm$ flow is produced near the star with a Lorentz factor $\gamma \gtrsim 10^3$ via continual discharge. As the outflow expands and fills the j-bundle, it experiences a radiative drag (deceleration) due to resonant scattering of thermal photons (with energies in the keV range) around the NS. Beloborodov (2013a, 2013b) showed that the Lorentz factor of the flow decreases proportionally to the local magnetic field

$$\gamma \sim 100 \frac{B}{B_Q}, \quad (8)$$

where $B_Q = m_e^2 c^3/\hbar e \simeq 4.44 \times 10^{13}$ G. Close to the star, where $B \gtrsim 10^{13}$ G, the energy of scattered photons,

$$E_{sc} \sim \gamma(B/B_Q) m_e c^2 \sim 50(B/B_Q)^2 \text{ MeV} \sim 5\gamma^2 \text{ keV}, \quad (9)$$

is large enough to immediately convert to $e^\pm$ pairs. At larger radii, where $B \lesssim 10^{13}$ G, the scattered photons escape, and the

Table 4
Best-fit Parameters for 1E 2259+586 for Phase-averaged and Phase-resolved Analysis

Phase	Data[a]	Energy (keV)	Fit Model[b]	N_H[c] ($\times 10^{22}$ cm^{-2})	kT (keV)	Γ_s/kT[d] (-/keV)	E_{break}[e] (keV)	Γ_h[f]	Flux[g]	Ratio[h]	χ^2/dof
0–1	S	0.5–10.0	BB+BB	0.60(4)	0.35(2)	0.71(6)	$\cdots$	$\cdots$	1.9(2)	1.00(1)	331/537
0–1	S	0.5–10.0	BB+PL	1.10(6)	0.42(2)	4.1(1)	$\cdots$	$\cdots$	2.1(1)	1.71(9)	402/537
0–1	S/N	0.5–79.0	BB+BB	0.60(4)	0.423(3)	1.78(4)	$\cdots$	$\cdots$	2.25(5)	0.2(1)	1448/827
0–1	S/N	0.5–79.0	BB+PL	1.10(6)	0.38(1)	3.91(3)	$\cdots$	$\cdots$	2.2(1)	2.5(3)	1152/827
0–1	S/N	0.5–79.0	BB+2PL	1.10(6)	0.410(7)	4.34(3)	$\cdots$	0.4(1)	2.36(7)	0.31(2)	689/825
0–1	S/N	0.5–79.0	BB+bPL	1.10(6)	0.409(9)	4.08(3)	11.5(3)	1.2(1)	3.0(1)	2.2(2)	747/825
Peak A	S/N	0.5–79.0	BB+2PL	1.10(6)	0.416(6)	4.57(7)	$\cdots$	1.0(3)	0.68(3)	0.29(4)	716/803
Peak B	S/N	0.5–79.0	BB+2PL	1.10(6)	0.399(5)	4.41(5)	$\cdots$	0.3(1)	0.73(3)	0.53(4)	645/812
Off-pulse	S/N	0.5–79.0	BB+2PL	1.10(6)	0.404(6)	4.87(9)	$\cdots$	1.0(4)	0.48(3)	0.37(6)	879/1031
Peak A	S/N	0.5–79.0	BB+bPL	1.10(6)	0.397(5)	4.37(4)	10.8(5)	1.38(1)	1.51(4)	0.78(2)	776/803
Peak B	S/N	0.5–79.0	BB+bPL	1.10(6)	0.386(5)	4.26(5)	10.9(4)	0.9(2)	1.46(2)	0.85(1)	696/812
Off-pulse	S/N	0.5–79.0	BB+bPL	1.10(6)	0.393(5)	4.66(5)	9.6(4)	1.4(4)	1.43(3)	0.47(1)	911/1031

Notes. Numbers in parentheses indicate the 1σ uncertainty in least significant digits. Cross-normalization factors were used when data from *NuSTAR* and *Swift* were combined. These factors were set to 1.0 for module A of *NuSTAR* and to 1 for *Swift* if no *NuSTAR* data were included. Cross-normalization factors were frozen to values obtained for phase-averaged spectral analysis, when performing phase-resolved spectral analysis simultaneously for *NuSTAR* and *Swift*. Fluxes are unabsorbed fluxes measured using XSPEC's `cflux` model.
[a] *NuSTAR* 5–79 keV (N), *Swift* 0.5–10 keV (S).
[b] Blackbody (BB), power law (PL), broken power law (bPL).
[c] N_H was frozen to the value obtained from the phase-averaged spectral analysis for the phase-resolved analysis.
[d] Soft photon index Γ_s if BB+PL model is used. Blackbody temperature of second (hot) BB if BB+BB is fit.
[e] Break energy for the broken power law (where applicable).
[f] Photon index of the hard power-law component.
[g] Unabsorbed flux in units of 10^{-11} erg cm^{-2} s^{-1} from 2–10 keV for *Swift* and 2–79 keV if *NuSTAR* data are included for all model components (BB+BB, BB+PL, BB+bPL) or two PL components (BB+2PL).
[h] Ratio of flux in the 2–10 keV range for *Swift* and 2–79 keV range if *NuSTAR* is included. We show $F_{BB(hot)}/F_{BB(cold)}$ (BB+BB), F_{PL}/F_{BB} (BB+PL), F_{bPL}/F_{BB} (BB+bPL) and $F_{PL(hard)}/F_{PL(soft)}$ (BB + 2PL).

flow radiates almost all its kinetic energy before it reaches the magnetic equator, where the $e^\pm$ pairs annihilate. The predicted hard X-ray spectrum has an average photon index of -1.5 (this follows from Equations (8) and (9)) and cuts off in the MeV band. The hard X-rays are beamed along the magnetic field lines, and the observed spectrum varies greatly depending on the line of sight (see Figure 7 in Beloborodov 2013b).

To fit the *NuSTAR* data, we make the simple assumption of an axisymmetric j-bundle. The poloidal magnetic field is assumed to be close to the dipole configuration, and the magnetic dipole moment is fixed to the value inferred from spin-down, $\mu_{sd} \simeq 5.9 \times 10^{31}$ G. The model is described by five parameters: (1) the angular position θ_j (magnetic colatitude) of the j-bundle footprint, (2) the angular width $\Delta\theta_j$ of the j-bundle footprint, (3) the power L of the $e^\pm$ outflow along the j-bundle, (4) the angle α_{mag} between the rotation axis and the magnetic axis, and (5) the angle β_{obs} between the rotation axis and the observer's line of sight. In addition, the reference point of the rotational phase, ϕ_0, must be introduced as a free parameter when fitting the phase-resolved spectra. Note that $\Delta\theta_j = \theta_j$ would describe a polar cap. In this paper, we allow the j-bundle to have a ring-shaped footprint, which corresponds to $\Delta\theta_j < \theta_j$.

To test observations against the model, we follow the two-step method proposed by Hascoët et al. (2014). We first explore the whole parameter space by fitting the phase-averaged spectrum of the total (pulsed+unpulsed) emission together with three phase-resolved spectra of the pulsed emission. We only consider data above 16 keV where the observed hard component starts to dominate over the soft component as apparent from Figure 7. The results are shown in Figure 8. We find that the model can fit the data. However, the fit does not give strong constraints on the parameters of the model; a large region in the $\alpha_{mag} - \beta_{obs}$
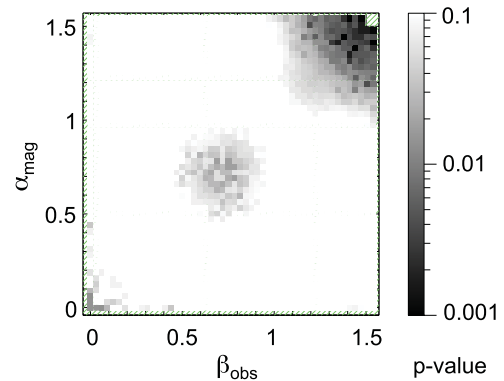
Figure 8. Map of p values for the fit of the hard X-ray component with the coronal outflow model. The p values are shown in the plane of (α_{mag}, β_{obs}) and maximized over the other parameters. The p value scale is shown on the right. While the hatched green region has p values smaller than 0.001, the white region has p values greater than 0.1. Low p values show parameters which are statistically disfavored (or excluded). Interchanging the values of α_{mag} and β_{obs} does not change the model spectrum, as long as the j-bundle is assumed to be axisymmetric. Therefore, the map of p values is symmetric about the line of $\beta_{obs} = \alpha_{mag}$.
(A color version of this figure is available in the online journal.)

plane is allowed. The only significant constraint derived from this analysis is that the polar-cap shape of the j-bundle footprint does not give a good fit; we find that a ring-shaped footprint is statistically preferred with $0.4 \lesssim \theta_j \lesssim 0.75$ and $\Delta\theta_j/\theta_j \lesssim 0.2$ (at the 1σ level).

At the second step, we freeze the best-fit parameters for the outflow model and fit the phase-averaged spectrum in the 0.5–79 keV range using both *NuSTAR* and *Swift* data. We test different models for the soft component, taking into account the

Table 5
Parameters of the Best-fit Model for the Soft X-Ray Component (*NuSTAR* and *Swift* Phase-averaged Spectra)

Model	N_H (10²² cm⁻²)	kT_1 (keV)	kT_2 (keV)	E_{tail} (keV)	L_1[a]	L_2[a]	Γ	νL_ν[a] @ 1 keV	χ^2/dof	*p* Value
BB+BB	0.44(2)	0.430(4)	1.22(2)	⋯	1.7(2)	0.073(3)	⋯	⋯	632/497	3.8×10^{-5}
BB+PL	1.17(4)	0.43(1)	⋯	⋯	0.6(1)	⋯	4.28(5)	3.3(3)	526/497	0.18
BB$_{tail}$	0.52(2)	0.401(6)	⋯	2.59(5)	1.13(9)	⋯	⋯	⋯	539/498	0.098
BB$_1$+ BB$_{tail,2}$	0.62(4)	0.33(3)	0.65(9)	4.3(6)	1.1(1)	0.3(2)	⋯	⋯	522/496	0.20

Note. [a] In units of $10^{35}(D/D_0)^2$ erg s⁻¹, where $D_0 = 4.0$ kpc is the distance inferred for 1E 2259+586 (Tian et al. 2010).

extension of the outflow contribution to low energies. Among these models BB$_{tail}$ is a phenomenological modification of the BB, where the Wien tail is replaced by a PL smoothly connected to the Planck distribution (see Hascoët et al. 2014). The energy E_{tail}, at which the PL starts, is a free parameter. All results are summarized in Table 5.

4. DISCUSSION

In this paper we report on observations of 1E 2259+586 in X-rays obtained with the *NuSTAR* and *Swift* satellites. We observe a double-peak structure above 24 keV for the first time at a statistical significance larger than 3σ. Furthermore we find a hint of a phase shift toward lower phase values for one of the peaks in the pulse profile. We also find the PF of 1E 2259+586 increases strongly with energy. To describe the phase-averaged total spectrum of the magnetar we use an absorbed BB plus a broken PL. Furthermore, we test the coronal outflow model of Beloborodov (2013a) using the observed phase-averaged and phase-resolved spectra.

4.1. Pulse Profile

The *NuSTAR* pulse profiles of 1E 2259+586 generally agree with those presented previously in Kuiper et al. (2006) based on *RXTE* data. A change in peak predominance occurs with increasing energy at the boundary between the high-energy end of the soft component (where thermal emission from the star is the dominant source) and the beginning of the hard component (where the $e^\pm$ outflow becomes the dominant source).

The two pulses of the double-peak profile seen in 1E 2259+586 are separated by half a period and have similar peak fluxes. This might be an indication that the NS is seen from the same magnetic latitude[18] (in absolute value) every half period (assuming that the emission pattern around the NS is relatively axisymmetric). This is possible if (and only if) $\alpha_{mag} \approx \pi/2$ (corresponding to a nearly orthogonal rotator) or $\beta_{obs} \approx \pi/2$. Note that no specific line of sight is a priori favored and $\beta_{obs} \approx \pi/2$ is the most probable observer angle. We also note that the center of pulse B shifts from 1.38 to 1.35(2) for energies above 8 keV, while the initially dominant peak A remains centered at the same phase independent of energy. The phase shift of peak B is, however, not significant with current statistics, and more data are needed to confirm or rule out the observed trend. The $e^\pm$ outflow and its emission are probably not perfectly axisymmetric, which can easily result in an energy-dependent phase shift of the peak maxima. Modeling such a minor shift with a small

number of parameters is difficult and would require a different, more complicated fitting procedure.

Both the area and the peak-to-peak PF as well as PF$_{rms}$ show an increase with energy. The area PF is about 60% for energies around 10 keV and rises to close to 100% at 20 keV, PF$_{rms}$ is around 30% and 70% at these energies, respectively. The *Swift* and *NuSTAR* values for area and peak-to-peak PF are consistent with those reported by Patel et al. (2001) as peak-to-peak PF for $E = 0.5$–7.0 keV of $35.8\% \pm 1.4\%$. The use of different analysis techniques precludes a direct comparison of the PFs we determined and those established in some previous publication (spectral PF of $\gtrsim 43\%$ for energies below 10 keV as reported by Kuiper et al. 2006). We can compare, however, the general behavior for the PF versus energy observed for 1E 2259+586 with that for other magnetars. Kuiper et al. (2006) reported an increase of PF with energy for 1E 1841−045, 4U 0142+61 and 1RXS J1708−4009. An et al. (2013) observed the same tendency for 1E 1841−045, although the trend was not quite as pronounced ($24\% \pm 4\%$ rms PF at 20 keV and $41\% \pm 18\%$ at 80 keV). For 1E 2259+586 we clearly see a dramatic increase in PF following the general trend observed for other magnetars. Such an increase in the PF is naturally expected in the coronal outflow model: photons of higher energy are more strongly beamed along the magnetic field lines as they are produced where the flow moves with a higher Lorentz factor (see Equation (9)).

4.2. Spectrum

We found that the spectral parameters of *Swift* and *NuSTAR* for the phase-averaged spectrum (see Section 3.2.1) agree well with those reported by Patel et al. (2001) and Zhu et al. (2008). These results support the fact that especially the soft-band spectrum (below $\sim$10 keV) has been stable over a period of $\sim$13 yr from *Chandra* observations in 2000 (Patel et al. 2001) to 2013 despite an antiglitch (Archibald et al. 2013) and glitches (Kaspi et al. 2003; Icdem et al. 2012), that temporarily altered the spectral parameters.

With the new data we were able to test if an additional PL component is required and find that it is. Therefore 1E 2259+586 exhibits the general tendency for magnetars to get harder at X-ray energies above 10 keV. We parameterized the *NuSTAR* plus *Swift* spectrum with a BB plus double PL model as well as a BB plus a broken PL. This phenomenological parameterization is a convenient way to characterize the presence of a hard X-ray component; the physical model of a coronal outflow is discussed in Section 4.3 below.

We note that the results of our analysis support the anticorrelation of spectral turnover ($\Gamma_s - \Gamma_h$) with magnetic field B and spin-down $\dot\nu$ suggested by Kaspi & Boydstun (2010). The authors demonstrated that there is a trend suggesting that those

---

[18] While the rotation axis of the neutron star is fixed, the orientation of the magnetic axis relative to the observer changes with phase if $\alpha_{mag} \neq 0$. As a result the magnetic latitude of the observer line of sight also changes with phase.
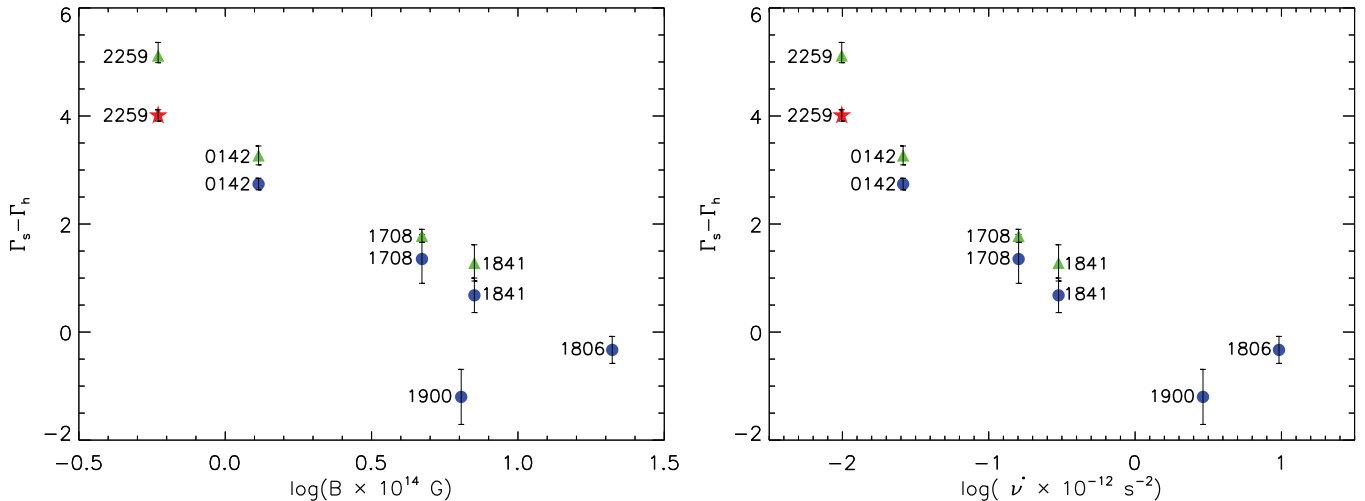
Figure 9. Spectral turnover ($\Gamma_s - \Gamma_h$) vs. magnetic field B (left) and spin-down $\dot{\nu}$ (right) from Kaspi & Boydstun (2010) for all magnetars presented there as well as our new result. Blue circles represent total flux, and green triangles represent pulsed flux. Our total flux result is indicated by the red star. 1σ uncertainties are shown. For details on the full list of magnetar names, included data, and references, see Kaspi & Boydstun (2010).

(A color version of this figure is available in the online journal.)

magnetars with the highest (lowest) B or $\dot{\nu}$ have the smallest (largest) spectral turnover. In Figure 9, we summarize the results of Kaspi & Boydstun (2010) for pulsed (green triangles) and total fluxes (blue circles) and add our new findings for 1E 2259+586 (red star) which further strengthens their case. Errors shown are 1σ uncertainties. It is interesting to point out that the observed spectral turnover for energetic rotation-powered pulsars (RPPs) is practically zero despite their much lower magnetic fields. Therefore Kaspi & Boydstun (2010) concluded that the production mechanism for X-rays above 10 keV in RPPs differs significantly from the one in magnetars. We also find a value for the hardness ratio, i.e., F_h/F_s (flux ratio of hard to soft spectral component in the 2–79 keV band), that agrees well with the observed correlation of hardness ratio and characteristic age that has been inferred from the spin-down rate, as reported by Enoto et al. (2010). They found a decrease in hardness ratio with increasing characteristic age or, likewise, an increase of F_h/F_s with magnetic field B.

Furthermore, we investigate the phase-resolved spectra for *NuSTAR* and *Swift* and find that the PL indices were slightly harder for peak B than for peak A, while the breaking point for the energy is located around 10 keV for both pulses. We also examine pulsed spectra extracted from the *NuSTAR* observation, but due to low statistics we are not able to rule out a single PL. More high-energy data are needed in order to compare the results to those of Kuiper et al. (2006).

We comment further that our analysis did not find any spectral lines or absorption features in the phase-averaged and phase-resolved spectra that could be interpreted as cyclotron lines (Tiengo et al. 2013). We also searched for short bursts in the data, but in contrast to 1E 1048.1−5937, for which recently six bright X-ray bursts have been reported in *NuSTAR* data (An et al. 2014), we did not observe a similar behavior for 1E 2259+586.

4.3. Spectral Modeling with the Coronal Outflow Model

We find that the phase-resolved spectra of 1E 2259+586 are consistent with the model of Beloborodov (2013a), although the available data do not allow us to derive strong constraints on the parameters of the model. In contrast to 1E 1841−045 (An et al. 2013), 4U 0142+61, and 1RXS J1708−4009 (Hascoët et al.

2014), a broad range of α_{mag} and β_{obs} is so far allowed for 1E 2259+586. The reason for this degeneracy is twofold: (1) the statistics of *NuSTAR* data of 1E 2259+586 are not as good as for the other objects; (2) the magnetic dipole moment of 1E 2259+586 is rather low, one order of magnitude smaller than for 1E 1841−045. As a result, the boundary of the radiative zone (where $B \sim 10^{13}$ G) is closer to the star. This leads to a larger allowed range of the j-bundle latitudes and to more flexible predictions of the model. Better statistics (with longer exposure times), extension of observations to the MeV range (where the emission of the $e^{\pm}$ outflow peaks), or polarization measurements would help to break the degeneracy of α_{mag} and β_{obs}.

The footprint location of the j-bundle is better constrained, with $0.4 \lesssim \theta_j \lesssim 0.75$ and $\Delta\theta_j/\theta_j \lesssim 0.2$ (at the 1σ level). This means that a ring-like footprint located at rather high co-latitudes[19] is statistically preferred to a polar cap footprint covering low colatitudes. This contrasts with the results obtained for 1E 1841−045 (An et al. 2013), 4U 0142+61, and 1RXS J1708−4009 (Hascoët et al. 2014), where a polar cap footprint provided a good fit. If confirmed with future, higher-statistics data, it would point to diversity in the crustal motions responsible for the twist of the magnetosphere.

We also analyzed the soft component, taking into account the extension of the outflow emission to low energies. The results are not very sensitive to the choice of parameters for the coronal outflow, because all good fits have similar extensions to low energies, which cut off below ∼5 keV. We find that the models BB+PL and BB+BB$_{tail}$ provide equally good fits to the soft component; the fit with a modified blackbody (BB$_{tail}$) is only slightly worse but still acceptable, while the two-blackbody model (BB+BB) is statistically unacceptable. Even though BB+PL provides a good fit, it is physically problematic because the PL component is brighter than the BB (at all frequencies) and its energy content diverges at the low-energy end of the spectrum (in case of no cut off). It likely overpredicts the (sub) keV flux and the hydrogen column density N_H. Our physically preferred model is BB+BB$_{tail}$, where the cold BB corresponds to emission

---

[19] Complementary angle of the latitude, i.e., difference between 90° and latitude.

from most of the NS surface and the hot modified BB to a hot spot on the star (Hascoët et al. 2014). Such a spot may be expected at the footprint of the j-bundle, as some particles produced in the $e^{\pm}$ discharge bombard the footprint and heat it (Beloborodov 2009). The area of the cold and hot thermal components are $\mathcal{A}_1 \approx 0.7\ \mathcal{A}_{\mathrm{NS}}$ and $\mathcal{A}_2 \approx 0.02\ \mathcal{A}_{\mathrm{NS}}$, respectively, where $\mathcal{A}_{\mathrm{NS}}$ represents the surface area of a NS with a typical radius of $R_{\mathrm{NS}} = 10$ km. These results are similar to those obtained for 1E 1841−045, 4U 0142+61, and 1RXS J1708−4009 (Hascoët et al. 2014). Note however that "BB$_{\mathrm{tail}}$ only" also provides an acceptable fit for the soft component in 1E 2259+586, and the parameters of the hot spot in this source are not strongly constrained from these data.

5. CONCLUSION

We present an analysis of simultaneous *NuSTAR* and *Swift* observations of the AXP 1E 2259+586, and report on our spectral and temporal results. We find that the double-peak pulse profile in different energy bands generally agrees with previous *RXTE* results, indicating a gradual change in peak dominance with energy. We used Fourier analysis techniques to quantify the similarities and differences and also show for the first time pulsations in the energy band above 24 keV for non-background-subtracted *NuSTAR* data. There is a hint at a change of position in phase for one of the two peaks in the pulse profile with increasing energy, but more data are needed to confirm this observation. This might suggest the pulsar is not a nearly orthogonal rotator. We also present the area and peak-to-peak PFs along with the rms variation, showing that they all increase with energy and reach 96% ± 14% (PF$_{\mathrm{area}}$) and 71% ± 15% (PF$_{\mathrm{rms}}$) at around 20 keV, similar to what is seen in other magnetars (Kuiper et al. 2006). The phase-averaged spectral analysis for the magnetar finds that there is good agreement between previous *Chandra* and *RXTE* data and the new observations. We also report that a model with an addition PL component (BB+2PL or BB+broken PL) is statistically preferred for the pulsar spectrum including the hard X-ray *NuSTAR* data. Our result for parameterization of the spectral turnover supports the anticorrelation hypothesis of Kaspi & Boydstun (2010) and we obtain a value of $\Gamma_s - \Gamma_h = 4.0(1)$ for $B = 0.59 \times 10^{14}$ G. Our findings also agree with the observed correlation of hardness ratio and characteristic age as reported by Enoto et al. (2010). The observed phase-resolved spectra are consistent with the coronal outflow model of Beloborodov (2013a). The fits of the spectra by the model prefer a ring-like j-bundle, in contrast to 1E 1841−045, 4U 0142+61, and 1RXS J1708−4009 (Hascoët et al. 2014). Unfortunately the available data do not provide significant constraints on the magnetic inclination (α_{mag}) or the observer line of sight (β_{obs}).

REFERENCES

An, H., Hascoët, R., Kaspi, V. M., et al. 2013, ApJ, 779, 163
An, H., et al. 2014, ApJ, submitted
Archibald, A. M., Dib, R., & Kaspi, V. M. 2007, CASCA, 2007, http://www.physics.mcgill.ca/∼aarchiba/pulsed-flux-CASCA-07.pdf
Archibald, R. F., Kaspi, V. M., Ng, C.-Y., et al. 2013, Natur, 497, 591
Beloborodov, A. M. 2009, ApJ, 703, 1044
Beloborodov, A. M. 2013a, ApJ, 762, 13
Beloborodov, A. M. 2013b, ApJ, 777, 114
Burrows, D. N., Hill, J. E., Nousek, J. A., et al. 2005, SSRv, 120, 165
Capalbi, M., Perri, M., Saija, B., Tamburelli, F., & Angelini, L. 2005, Technical Report 1.2, The Swift XRT Data Reduction Guide, http://swift.gsfc.nasa.gov/analysis/xrt_swguide_v1_2.pdf
De Jager, O. C., Swanepoel, J. W. H., & Raubenheimer, B. C. 1989, A&A, 221, 180
Den Hartog, P. R., Hermsen, W., Kuiper, L., et al. 2006, A&A, 451, 587
Dib, R., & Kaspi, V. M. 2014, ApJ, 784, 37 (arXiv:1401.3085)
Durant, M., & van Kerkwijk, M. H. 2006, ApJ, 650, 1082
Enoto, T., Nakazawa, K., Makishima, K., et al. 2010, ApJL, 722, L162
Fahlman, G. G., & Gregory, P. C. 1981, Natur, 293, 202
Fahlman, G. G., & Gregory, P. C. 1983, in IAU Sym. 101, Supernova Remnants and Their X-ray Emission, ed. J. Danziger & P. Gorenstein (Dordrecht: Reidel), 445
Gavriil, F. P., Kaspi, V. M., & Woods, P. M. 2002, Natur, 419, 142
Gehrels, N., Chincarini, G., Giommi, P., et al. 2004, ApJ, 611, 1005
Gonzalez, M. E, Dib, R., Kaspi, V. M., et al. 2010, ApJ, 716, 1345
Hailey, C. J., An, H., Blaedel, K. L., et al. 2010, Proc. SPIE, 7732, 77320T
Harrison, F. A., Cook, W. R., Miyasaka, H., & McLean, R. 2010, in Semiconductor Radiation Detection Systems, ed. K. Iniewsk (Boca Raton, FL: CRC Press), 67
Harrison, F. A., Craig, W. W., Christensen, F. E., et al. 2013, ApJ, 770, 103
Hascoët, R., Beloborodov, A. M., & den Hartog, P. R. 2014, ApJL, 786, L1
Icdem, B., Baykal, A., & Inam, S. C. 2012, MNRAS, 419, 3109
Kaspi, V. M., & Boydstun, K. 2010, ApJL, 710, L115
Kaspi, V. M., Chakrabarty, D., & Steinberger, J. 1999, ApJL, 525, L33
Kaspi, V. M., Gavriil, F. P., Woods, P. M., et al. 2003, ApJL, 588, L93
Kuiper, L., Hermsen, W., den Hartog, P. R., & Collmar, W. 2006, ApJ, 645, 556
Olausen, S. A., & Kaspi, V. M. 2014, ApJS, 212, 6
Patel, S. K., Kouveliotou, C., Woods, P. M., et al. 2001, ApJL, 563, L45
Sasaki, M., Plucinsky, P. P., Gaetz, T. J., et al. 2004, ApJ, 617, 322
Thompson, C., & Duncan, R. C. 1993, ApJ, 408, 194
Thompson, C., & Duncan, R. C. 1996, ApJ, 473, 322
Tian, W. W., Leahy, D. A., & Li, D. 2010, MNRAS, 404, L1
Tiengo, A., Esposito, P., Mereghetti, S., et al. 2013, Natur, 500, 312
Wik, D., Hornstrup, A., Molendi, S., et al. 2014, ApJ, submitted (arXiv:1403.2722)
Woods, P. M., Kaspi, V. M., Thompson, C., et al. 2004, ApJ, 605, 378
Zhu, W., Kaspi, V. M., Dib, R., et al. 2008, ApJ, 686, 520